Jiaven Xu[1]
Jiangsu Key Lab of Remote
Measurement and Control,
School of Instrument Science and Engineering,
Southeast University,
Jiangsu 210096, China
e-mail: jiawen.xu@seu.edu.cn

Guobiao Hu
Department of Mechanical Engineering,
University of Auckland,
20 Symonds Street,
Auckland 1010, New Zealand
e-mail: ghu211@aucklanduni.ac.nz

Lihua Tang[1]
Department of Mechanical Engineering,
University of Auckland,
20 Symonds Street,
Auckland 1010, New Zealand
e-mail: l.tang@auckland.ac.nz

Yumin Zhang
Zhejiang Institute of Research and Innovation,
The University of Hong Kong,
Zhejiang 311305, China
e-mail: yumin@connect.hku.hk

Ruqiang Yan
International Machinery Center,
School of Mechanical Engineering,
Xi'an Jiaotong University,
Shaanxi 710049, China
e-mail: Ruqiang@seu.edu.cn

Modeling and Analysis of Phononic Crystal With Coupled Lanes for Enhanced Elastic Wave Attenuation

Phononic crystals and metamaterials have attractive potential in elastic wave attenuation and guiding over specific frequency ranges. Different from traditional phononic crystals/metamaterials consisting of identical unit cells, a phononic crystal with coupled lanes is reported in this article for enhanced elastic wave attenuation in the low-frequency regime. The proposed phononic crystal takes advantages of destructive interference mechanism. A finitely length phononic crystal plate consisting of coupled lanes is considered for conceptual verification. The coupled lanes are designed to split the incident elastic wave into separated parts with a phase difference to produce destructive interference. Theoretical modeling and finite element method (FEM) analysis are presented. It is illustrated that significant elastic wave attenuation is realized when the phase difference of elastic waves propagating through the coupled lanes approximates π. Besides, multiple valleys in the transmission can be achieved in a broad frequency range with one at a frequency as low as 1.85 kHz with unit cells' width and length of 25 mm and ten unit cells in one lane.

[DOI: 10.1115/1.4048394]

Keywords: phononic crystal, dispersion relation modulation, destructive interference, elastic wave attenuation, dynamics, materials in vibration and acoustics, structural dynamics and control, vibration control

1 Introduction

Phononic crystals (PCs) and metamaterials with artificially designed periodic structures have attracted intensive attention due to their promising advantages in wave manipulation and attenuation [1–8]. PCs and metamaterials have applications of negative refraction [9,10], acoustic cloaking [3,5], wave focusing [11–15], wave attenuation [4,7,16], and vibration mode tailoring [17]. Moreover, dispersion curves of PCs and metamaterials may exhibit a negative slope, yielding negative refraction phenomenon [9,10]. The unique features of phononic crystals and metamaterials are originated from the mechanisms of Bragg scattering and local resonance, respectively [2,10,18,19]. The Bragg scattering phenomenon occurs when the elastic wavelength is comparable with the dimension of the unit cell [20–22]. Since the wavelength is roughly inversely proportional to the frequency of elastic wave, the application of PCs in the low-frequency regime requires large-size unit cells. On the other hand, metamaterials, which take advantages of the local resonance behavior rather than the Bragg scattering, possess extraordinary capability of manipulating low-frequency elastic waves at sub-wavelength scales [1,23–25].

Extensive efforts have been devoted to attenuating elastic wave using PCs and metamaterials. For example, a low-frequency bandgap would be generated in the vicinity of the resonating frequency of the local resonators periodically integrated in the primary structures. The generated bandgap in such a kind of metamaterials exhibited a strong vibration attenuation effect. Explorations were carried out for the vibration control in structural bars and beams [7,8,21,26]. The bandgap width of the metamaterial was demonstrated to be expandable by parametric optimization [7]. Normally, the mechanical metamaterials and PCs have fixed bandgap behavior [6–8]. To introduce online tunability, piezoelectric transducers have been adopted due to their two-way electromechanical coupling [16,27]. A negative capacitance element, a nonresonating shunt circuit, was integrated in the piezoelectric unit cell to reduce the equivalent local stiffness, thereby adjusting the Bragg scatting bandgap features through modifying the value of the negative capacitance [28]. Alternatively, piezoelectric metamaterial with unit cell level LC resonating can produce directly the bandgap. For example, periodic piezoelectric transducers with inductance shunt circuits are integrated into rod for wave attenuation [22,29]. Piezoelectric phononic crystals and metamaterials with shunt circuits have advantages over the mechanical one in two aspects of simple configuration and adaptivity. The external shunt circuits connected to the piezoelectric transducers allow online tuning of bandgap toward a desired frequency range without modifying the mechanical designs of the system.

The recent concept of metasurface provides great promise in the modulation of elastic waves [27,30–37]. Wavefronts of the elastic waves propagating through a sheet-like region are artificially engineered. Different from the bulk phononic crystal and metamaterial, metasurfaces are more compact but can realize similar functionalities in elastic wave guiding by altering the phase gradient at the sub-wavelength scale. Modulated acoustic waves propagations by metasurfaces have been investigated intensively. For example, labyrinthine unit-based metasurface was adopted for realizing

---

[1] Corresponding authors.

Contributed by the Design Engineering Division of ASME for publication in the Journal of Vibration and Acoustics. Manuscript received April 22, 2020; final manuscript received August 5, 2020; published online October 5, 2020. Assoc. Editor: Fabio Semperlotti.

anomalous reflection, ultrathin planar lenses, and nonparaxial beams [27,30]. Elastic metasurfaces built upon geometric tapers are proposed for accomplishing the anomalous refraction of guided waves in solids [36]. Metasurfaces for controlling lamb waves with and without mode conversion in plates were demonstrated by theoretically and experimentally analysis. For the sake of controlling bulk waves without involving mode conversion, a metasurface with an array of aligned parallel cracks in a bulk elastic medium is designed to split SV- and P-waves in elastic solids into different propagation directions [38]. In general, existing designs of metasurfaces are focusing on wave guiding.

Conversely, the application of PCs and metamaterials in the field of wave attenuation is largely restricted by their narrow bandwidths. To overcome this limitation, efforts have been devoted into achieving bandgap enlargement. Multiple local resonators were assembled in a unit cell of metamaterial to generate multiple bandgaps [23,26]. It was also demonstrated that the mechanical connection between adjunct unit cells can effectively enlarge the bandgap width of the elastic metamaterial [39]. Moreover, tunable wave attenuation is highlighted in the piezoelectric phononic crystal/ metamaterial for applications at a wide frequency range. For instance, the effectiveness of the negative capacitance circuit was experimentally proved in expanding the bandgap in a metamaterial system [28]. Unit cell level optimization of a piezoelectric metamaterial was performed, and it was demonstrated that the enhancement of electromechanical coupling could widen the bandgap width [40]. More recently, it was illustrated that incorporating nonlinearities into the local resonators of elastic metamaterials is an alternative strategy to broaden the bandgap [41–43].

In this study, we propose a PC plate with coupled lanes that exhibits promising wave attenuation capability. The key of the proposed system lies in producing different phase shifts of elastic waves in the separated lanes. A proper tuning of the phase difference results in the destructive interference phenomenon that yields enhanced wave attenuation in aspects of bandwidth and depth. The rest of this article is organized as follows. In Sec. 2, the concept of the PC with coupled lanes is outlined. In Sec. 3, governing equation of a unit cell is derived, and a finite element model is presented for evaluation of the dispersion relation of the unit cells. In Sec. 4, phase shift characteristics of the lanes are investigated. Section 5 provides the correlated analysis for validation and insights of the wave attenuation features of the PC with coupled lanes. Concluding remarks are presented in Sec. 6.

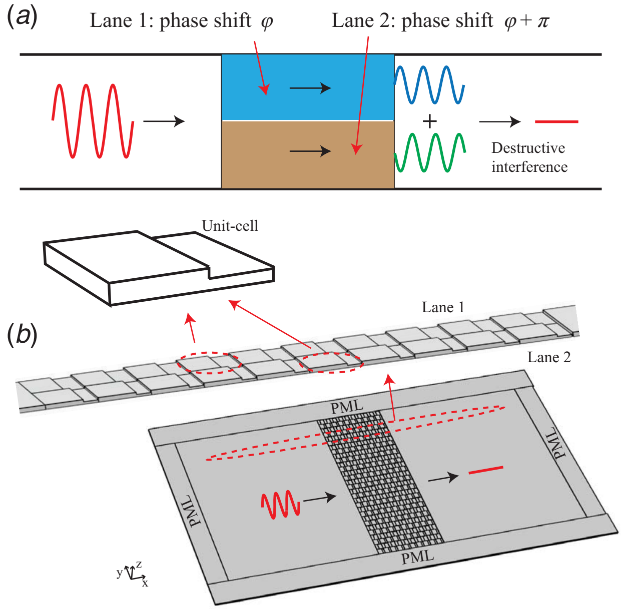

Fig. 1 **(*a*) Conceptual illustration of wave attenuation mechanism and (*b*) proposed PC system and the unit cell**

2 Conceptual Illustration

Figure 1 shows the proposed PC plate that consists of a series of coupled PC lanes. Unlike the traditional systems based on local resonance or Bragg scattering (a destructive interference in the direction of wave propagation) mechanisms, the proposed system takes advantages of destructive interference stemming from the phase shift difference between the coupled lanes constructed in the orthogonal direction of wave propagation. Destructive interference has been widely adopted in the design of antenna for directional wave minimization in the existing literature [44,45]. In analogy to the application for electromagnetic waves, here we introduce the mechanism of destructive interference for elastic wave attenuation. The underlying physics is that the incident elastic wave is split and passes through the lanes in the plate with respective phase shifts (Fig. 1(*a*)). The phase shifts of the waves in the adjacent lanes can be intentionally designed to meet the condition for destructive interference, resulting in the wave self-cancellation for vibration attenuation. For the sake of demonstration, we start from the equations of elastic waves in two adjacent lanes. The application of Bloch theorem allows to characterize the elastic wave in the two adjacent lanes in the following equation [46,47]:

$$\begin{aligned}\mathbf{u}_1(\mathbf{x}_1,\mathbf{k}_1,t)+\mathbf{u}_2(\mathbf{x}_2,\mathbf{k}_2,t)&=\tilde{\mathbf{u}}_1(\mathbf{x}_1,\mathbf{k}_1)\\ e^{i(\mathbf{k}_1\cdot\mathbf{x}_1-\omega t+\varphi_1)}&+\tilde{\mathbf{u}}_2(\mathbf{x}_2,\mathbf{k}_2)e^{i(\mathbf{k}_2\cdot\mathbf{x}_2-\omega t+\varphi_2)}\end{aligned} \tag{1}$$

where $\mathbf{u}_1$ and $\mathbf{u}_2$ denote the displacement fields of the elastic waves in two adjacent lanes, respectively. $\tilde{\mathbf{u}}_1$ and $\tilde{\mathbf{u}}_2$ stand for the Bloch displacement function with the periodicity of the unit cells; $\mathbf{x}_1$, $\mathbf{x}_2$, $\mathbf{k}_1$, $\mathbf{k}_2$, φ_1, φ_2, ω, and t denote position vector in lane 1, position vector in lane 2, wavevector of the elastic wave in lane 1, wavevector of the elastic wave in lane 2, phase elastic wave in lane 1, phase elastic wave in lane 2, operating frequency and time, respectively. It is worth noticing that the incident waves in the two adjacent lanes have the same operating frequency and the amount of mechanical energy, i.e., they have very close amplitudes of displacements and wavenumbers. At the location $\mathbf{x}_0$ where the elastic wave converges, Eq. (1) becomes

$$\begin{aligned}(\mathbf{u}_1(\mathbf{x}_1,\mathbf{k}_1,t)+\mathbf{u}_2(\mathbf{x}_2,\mathbf{k}_2,t))|_{\mathbf{x}_{1,2}=\mathbf{x}_0}&=(\tilde{\mathbf{u}}_1(\mathbf{x}_0,\mathbf{k}_1)e^{i\varphi_1}\\ &+\tilde{\mathbf{u}}_2(\mathbf{x}_0,\mathbf{k}_2)e^{i\varphi_2})e^{i(\mathbf{k}_2\cdot\mathbf{x}_0-\omega t)}\end{aligned} \tag{2}$$

Consider the fact that elastic waves in the two lanes have the same operating frequency and similar amplitudes and wavenumbers. Equation (2) yields

$$\begin{aligned}&(\tilde{\mathbf{u}}_1(\mathbf{x}_0,\mathbf{k}_1)e^{i\varphi_1}+\tilde{\mathbf{u}}_2(\mathbf{x}_0,\mathbf{k}_2)e^{i\varphi_2})e^{i(\mathbf{k}_2\cdot\mathbf{x}_0-\omega t)}\\ &\approx\tilde{\mathbf{u}}(\mathbf{x}_0,\mathbf{k})(e^{i\varphi_1}+e^{i\varphi_2})e^{i(\mathbf{k}\cdot\mathbf{x}_0-\omega t)}\end{aligned} \tag{3}$$

It is worth noticing that the elastic waves in lane 1 and 2 form a combined elastic wave at the location $\mathbf{x}_0$. That is, the elastic waves yield one wave with a single wavevector of $\mathbf{k}$. It can be obtained from Eq. (3) that the amplitude of the elastic wave passing through the PC region is a function of the difference of their phases. Notably, the value of Eq. (3) would be minimized when $|\varphi_1-\varphi_2|$ approximates π. In other words, the elastic wave would be self-cancellated when the waves in the adjacent lanes have a phase difference of π, as conceptually illustrated in Fig. 1(*a*). Therefore, the elastic wave has the potential to be attenuated by dispersion relation modulation in the PC lanes.

Without loss of generality, we assemble the proposed PC plate using coupled lanes consisting of staired unit cells (Fig. 1(*b*)). The staired unit cell is a stair-shaped beam synthesized by two segments. Each of the unit cells has the width and length of 25 mm. Besides, the staired unit cell has the height of 3 mm in one of the segments and various values in the other segment. The dimensions of the unit cells can be chosen at other values, whereas the underlying physics should be kept the same. Identical staired unit cells are connected in series to form one coupled PC lane. A small gap with the width of 0.1 mm is introduced between the PC lanes to reduce interactions between the lanes. Moreover, we coupled two adjacent lanes together and assemble many pairs of coupled lanes in parallel to form the PC plate. Each lane is formed by unit cells with different dimensions, i.e., different dispersion relations and phase shift features. The difference of phase shifts would then produce the wave attenuation effects.

3 Theoretical Modeling of a Unit Cell

As demonstrated in Sec. 2, the key feature of the proposed system to yield wave attenuation comes from the phase difference of elastic waves passing through PC lanes. For the sake of analyzing the phase shift characteristics that can facilitate wave attenuation, dispersion relation of a unit cell is formulated. The Euler–Bernoulli beam theory is used to consider the transverse wave in the beam-like lane. The staired unit cell of an individual lane contains two rectangular segments (Fig. 2). Let l_1, l_2, b, h_1, h_2, and ρ denote length of segment I, length of segment II, width, thickness of segment I and segment II, and mass density of the unit cell, respectively. In the following analysis, the unit cell length, i.e., $l_1 + l_2$ is fixed as a constant.

In the modeling of the unit cell, i indicates the ith segment of the staired unit cell. The Euler beam theory is employed to formulate the eigenvalue problem. In the mathematical modeling, the left edge of the unit cell locates at x_0. The governing equation of the unit cell is given as follows [17]:

$$\frac{\partial}{\partial x^2}\left[EI_i\frac{\partial^2 w(x,\,t)}{\partial x^2}\right]+\frac{\partial}{\partial t}\left[\rho A_i\frac{\partial w(x,\,t)}{\partial t}\right]=0,\quad i=1,2 \tag{4}$$

where EI_i is the bending stiffness of the ith segment of the unit cell and ρA_i is the mass per unit length of the ith segment ($i = 1, 2$). Here, $EI_i = (1/12)Ebh_i^3$ is a function of the thickness of the ith segment of the unit cell. $A_i = bh_i$ is for the area of the cross section of the beam. Let the displacement field of the unit cell be represented as follows:

$$w_i(x,\,t)=\phi_i(x)q(t) \tag{5}$$

where $\phi_i(x)$ is the general expression of displacement field of the unit cell.

$$\begin{aligned}\phi_1(x)=&A_1\cos\lambda_1(x-x_0)+B_1\sin\lambda_1(x-x_0)\\&+C_1\cosh\lambda_1(x-x_0)+D_1\sinh\lambda_1(x-x_0)\end{aligned} \tag{6a}$$

$$\begin{aligned}\phi_2(x)=&A_2\cos\lambda_2(x-l_1-x_0)+B_2\sin\lambda_2(x-l_1-x_0)\\&+C_2\cosh\lambda_2(x-l_1-x_0)+D_2\sinh\lambda_2(x-l_1-x_0)\end{aligned} \tag{6b}$$

In Eqs. (6a) and (6b), A_i, B_i, C_i, and D_i are coefficients that determine the displacement field of the unit cell. λ_i is related to the eigenfrequency ω as $\lambda_i=\sqrt[4]{\omega^2\frac{\rho A_i}{EI_i}}$, i.e., the eigenvalues here are functions of the length and thickness of the unit cell in segment I and II. Applying the Bloch theorem yields the periodic boundary conditions at the two ends of the unit cell, i.e., at x_0 and $x_0 + l_1 + l_2$:

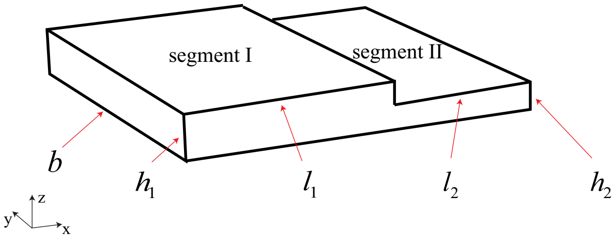

Fig. 2 Schematic of staired unit cell in the proposed PC lane

$$\phi_1(x_0)=e^{-ik_x(l_1+l_2)}\phi_2(x_0+l_1+l_2) \tag{7a}$$

$$\left.\frac{d\phi_1(x)}{dx}\right|_{x=x_0}=e^{-ik_x(l_1+l_2)}\left.\frac{d\phi_2(x)}{dx}\right|_{x=x_0+l_1+l_2} \tag{7b}$$

$$EI_1\left.\frac{d^2\phi_1(x)}{dx^2}\right|_{x=x_0}=e^{-ik_x(l_1+l_2)}EI_2\left.\frac{d^2\phi_2(x)}{dx^2}\right|_{x=x_0+l_1+l_2} \tag{7c}$$

$$EI_1\left.\frac{d^3\phi_1(x)}{dx^3}\right|_{x=x_0}=e^{-ik_x(l_1+l_2)}EI_2\left.\frac{d^3\phi_2(x)}{dx^3}\right|_{x=x_0+l_1+l_2} \tag{7d}$$

where k_x is the wavenumber in ΓX-direction that varies for different PC lanes. Substituting Eq. (6) into Eq. (7) gives

$$\begin{aligned}(A_1+C_1)e^{ik_x(l_1+l_2)}=&A_2\cos\lambda_2l_2+B_2\sin\lambda_2l_2\\&+C_2\cosh\lambda_2l_2+D_2\sinh\lambda_2l_2\end{aligned} \tag{8a}$$

$$\begin{aligned}(B_1\lambda_1+D_1\lambda_1)e^{ik_x(l_1+l_2)}=&-A_2\lambda_2\sin\lambda_2l_2+B_2\lambda_2\cos\lambda_2l_2\\&+C_2\lambda_2\sinh\lambda_2l_2+D_2\lambda_2\cosh\lambda_2l_2\end{aligned} \tag{8b}$$

$$\begin{aligned}EI_1(-A_1\lambda_1^2+C_1\lambda_1^2)e^{ik_x(l_1+l_2)}=&EI_2(-A_2\lambda_2^2\cos\lambda_2l_2-B_2\lambda_2^2\sin\lambda_2l_2\\&+C_2\lambda_2^2\cosh\lambda_2l_2+D_2\lambda_2^2\sinh\lambda_2l_2)\end{aligned} \tag{8c}$$

$$\begin{aligned}EI_1(-B_1\lambda_1^3+D_1\lambda_1^3)e^{ik_x(l_1+l_2)}=&EI_2(A_2\lambda_2^3\sin\lambda_2l_2-B_2\lambda_2^3\cos\lambda_2l_2\\&+C_2\lambda_2^3\sinh\lambda_2l_2+D_2\lambda_2^3\cosh\lambda_2l_2)\end{aligned} \tag{8d}$$

In addition, the continuity conditions of the deflection, slope, bending moment, and shear force at the conjunction of segment I and II in the unit cell, i.e., at $x_0 + l_1$, yield the following four equations:

$$\phi_1(x_0+l_1)=\phi_2(x_0+l_1)| \tag{9a}$$

$$\left.\frac{d\phi_1(x)}{dx}\right|_{x=x_0+l_1}=\left.\frac{d\phi_2(x)}{dx}\right|_{x=x_0+l_1} \tag{9b}$$

$$EI_1\left.\frac{d^2\phi_1(x)}{dx^2}\right|_{x=x_0+l_1}=EI_2\left.\frac{d^2\phi_2(x)}{dx^2}\right|_{x=x_0+l_1} \tag{9c}$$

$$EI_1\left.\frac{d^3\phi_1(x)}{dx^3}\right|_{x=x_0+l_1}=EI_2\left.\frac{d^3\phi_2(x)}{dx^3}\right|_{x=x_0+l_1} \tag{9d}$$

which yield

$$\begin{aligned}&A_1\cos\lambda_1l_1+B_1\sin\lambda_1l_1+C_1\cosh\lambda_1l_1\\&+D_1\sinh\lambda_1l_1=A_2+C_2\end{aligned} \tag{10a}$$

$$\begin{aligned}&-A_1\lambda_1\sin\lambda_1l_1+B_1\lambda_1\cos\lambda_1l_1+C_1\lambda_1\sinh\lambda_1l_1\\&+D_1\lambda_1\cosh\lambda_1l_1=B_2\lambda_2+D_2\lambda_2\end{aligned} \tag{10b}$$

$$\begin{aligned}&EI_1(-A_1\lambda_1^2\cos\lambda_1l_1-B_1\lambda_1^2\sin\lambda_1l_1\\&+C_1\lambda_1^2\cosh\lambda_1l_1+D_1\lambda_1^2\sinh\lambda_1l_1)=EI_2(-A_2\lambda_2^2+C_2\lambda_2^2)\end{aligned} \tag{10c}$$

$$EI_1(A_1\lambda_1^3 \sin\lambda_1 l_1 - B_1\lambda_1^3 \cos\lambda_1 l_1 + C_1\lambda_1^3 \sinh\lambda_1 l_1 + D_1\lambda_1^3 \cosh\lambda_1 l_1) = EI_2(-B_2\lambda_2^3 + D_2\lambda_2^3) \tag{10d}$$

The following eigenvalue problem is formulated by grouping Eqs. (8a)–(8d) and (10a)–(10d) together regarding the coefficients of the displacement field $\mathbf{d} = [A_1\ B_1\ C_1\ D_1\ A_2\ B_2\ C_2\ D_2]^{\mathrm{T}}$, i.e.,

$$\mathbf{K}(\lambda_1, \lambda_2)\mathbf{d} = 0 \tag{11}$$

where

$$\mathbf{K}(\lambda_1, \lambda_2) = \begin{bmatrix} \cos\lambda_1 l_1 & \sin\lambda_1 l_1 & \cosh\lambda_1 l_1 & \sinh\lambda_1 l_1 & -1 & 0 & -1 & 0 \\ -\lambda_1 \sin\lambda_1 l_1 & \lambda_1 \cos\lambda_1 l_1 & \lambda_1 \sinh\lambda_1 l_1 & \lambda_1 \cosh\lambda_1 l_1 & 0 & -\lambda_2 & 0 & -\lambda_2 \\ -EI_1\lambda_1^2 \cos\lambda_1 l_1 & -EI_1\lambda_1^2 \sin\lambda_1 l_1 & EI_1\lambda_1^2 \cosh\lambda_1 l_1 & EI_1\lambda_1^2 \sinh\lambda_1 l_1 & EI_2\lambda_2^2 & 0 & -EI_2\lambda_2^2 & 0 \\ EI_1\lambda_1^3 \sin\lambda_1 l_1 & -EI_1\lambda_1^3 \cos\lambda_1 l_1 & EI_1\lambda_1^3 \sinh\lambda_1 l_1 & EI_1\lambda_1^3 \cosh\lambda_1 l_1 & 0 & EI_2\lambda_2^3 & 0 & -EI_2\lambda_2^3 \\ e^{ik_x(l_1+l_2)} & 0 & e^{ik_x(l_1+l_2)} & 0 & -\cos\lambda_2 l_2 & -\sin\lambda_2 l_2 & -\cosh\lambda_2 l_2 & -\sinh\lambda_2 l_2 \\ 0 & \lambda_1 e^{ik_x(l_1+l_2)} & 0 & \lambda_1 e^{ik_x(l_1+l_2)} & \lambda_2 \sin\lambda_2 l_2 & -\lambda_2 \cos\lambda_2 l_2 & -\lambda_2 \sinh\lambda_2 l_2 & -\lambda_2 \cosh\lambda_2 l_2 \\ -EI_1\lambda_1^2 e^{ik_x(l_1+l_2)} & 0 & EI_1\lambda_1^2 e^{ik_x(l_1+l_2)} & 0 & EI_2\lambda_2^2 \cos\lambda_2 l_2 & EI_2\lambda_2^2 \sin\lambda_2 l_2 & -EI_2\lambda_2^2 \cosh\lambda_2 l_2 & -EI_2\lambda_2^2 \sinh\lambda_2 l_2 \\ 0 & -EI_1\lambda_1^3 e^{ik_x(l_1+l_2)} & 0 & EI_1\lambda_1^3 e^{ik_x(l_1+l_2)} & -EI_2\lambda_2^3 \sin\lambda_2 l_2 & EI_2\lambda_2^3 \cos\lambda_2 l_2 & -EI_2\lambda_2^3 \sinh\lambda_2 l_2 & -EI_2\lambda_2^3 \cosh\lambda_2 l_2 \end{bmatrix} \tag{12}$$

For a given length of segment I and II in the unit cell and a chosen operating frequency, we obtain the characteristic equation by letting the determinant $\mathbf{K}(\lambda_1, \lambda_2) = 0$ and then solve the eigenvalues λ_1 and λ_2 for the dispersion relation of the unit cell. The solutions can be solved numerically, and the dispersion relation of the unit cell can be determined. It is worth noticing that the dispersion relation of the unit cell is a function of length of the two segments. The wavenumber and phase characteristics of the unit cell can be modified through the length modulation of the two segments.

4 Dispersion Relation and Phase Modulation

4.1 Dispersion Relation of a Single Unit Cell. In this section, we proceed to analyze the dispersion relation of such a unit cell. Theoretical modeling and finite element software COMSOL 5.4 are adopted in the analysis. The finite element tool has been widely used in the investigations of PCs and metamaterials [22–30,48]. The unit cell is formed by an aluminum beam with different lengths and thicknesses in segments I and II, respectively. In the following analysis, the thickness of segment I (h_1) is kept constant as 3 mm. Three cases are considered that the thicknesses of segment II (h_2) have values of 1.5 mm, 2 mm, and 2.5 mm, respectively. In all of the three cases, the unit cell length is fixed at a constant value of 25 mm, i.e., $l_1 + l_2 \equiv 25$ mm. Besides, the width of the unit cell (b) has a constant value of 25 mm. Notably, the width b is an irrelevant parameter of the calculation as the dispersion of the unit cell would be kept the same when changing its width. It is worth mentioning that the parameters of the unit cell were arbitrarily chosen for the demonstration of the proposed concept. Unit cells can be set at other dimensions for the realization of the destructive interference. Besides, the elastic wave has a wavelength of 10.68 mm at 5 kHz for unit cells with $l_1 = 7.62$ mm and $h_2 = 2$ mm. The material mass density and Young's modulus are $\rho = 2730$ kg/m^3 and $E = 62$ GPa, respectively. We explore the dispersion relation of the unit cell in the first Brillouin zone by sweeping the wavenumber k_x from 0 to $\pi/(l_1 + l_2)$. To exclude the wave attenuation effects owing to bandgap, in this study, we choose an operating frequency of 5 kHz, which is below the Bragg scattering bandgaps of the unit cells. It is worth mentioning that the operating frequency can be chosen at any other frequency point where wave attenuation is desired to be achieved. The dispersion curves of the unit cells with representative lengths of segment I (l_1) are given.

Dispersion curves of the unit cells with $h_2 = 2$ mm and $l_1 = 24$ mm, 20 mm, and 16 mm are, respectively, given in Fig. 3(a). Both results from the theoretical modeling and finite element method (FEM) simulation are provided. The operating frequency 5 kHz is marked with a dashed line. It can be observed that the dispersion relation of the unit cell is shifted by changing l_1. In other words, the incident elastic wave at a selected frequency is shortened or stretched by decreasing or increasing the length of segment I in this staired unit cell. The shifting of dispersion relation implies the possibility of phase modulation of the elastic wave propagating through the medium. The relation of wavenumber and l_1 at 5 kHz is presented in Fig. 3(b). As illustrated in this figure, the value of the wavenumber of the unit cell at 5 kHz decreases as we increase the length of segment I. Due to the fact that the wavenumber is reversely proportional to the phase shift of the elastic wave within a unit cell, the phase shift would be a function of l_1. In other words, it implies the potential to achieve the expected destructive interference through parametric modification of the unit cells. Minor difference between the theoretical modeling and the FEM simulation is shown in Fig. 3(a) in the vicinity of $k_x = 120$/m. This is because the Euler beam assumption of the unit cell does not hold the actual situation in such a range. Overall, the theoretical predictions match the FEM simulations very well in the range of interest.

The wavenumber of the unit cell at 5 kHz is also a function of the thicknesses of segment II, as shown in Fig. 4. In this figure, the wavenumber of the unit cell with various l_1 is evaluated given different thicknesses of segment II, e.g., the values of h_2 are chosen as 1.5 mm, 2 mm, and 2.5 mm, respectively. The results are also obtained from both the theoretical calculations and FEM simulations at 5 kHz. As shown, the value of wavenumber of the unit cells decreases with the increase of l_1. Reducing the value of h_2 can effectively increase the wavenumbers of the unit cell. Furthermore, with the increase of h_2, the relation curve becomes flatter, which indicates a smaller wavenumber tuning range. Since the wavenumber shift corresponds to the phase shift of elastic wave, a unit cell with a smaller h_2 offers a larger tunability range of the phase shift by changing l_1. The results from the FEM simulation confirm the theoretical calculations.

4.2 Phase Modulation. In this section, phase shift characteristics of the PC are described. Noting the fact that phase shift within one unit cell is limited, we evaluate phase shift features of PC lanes with multiple unit cells in the following analysis. In particular, a single functional lane formed by one, five, and ten identical unit cells serially are analyzed to understand the phase shift modulation

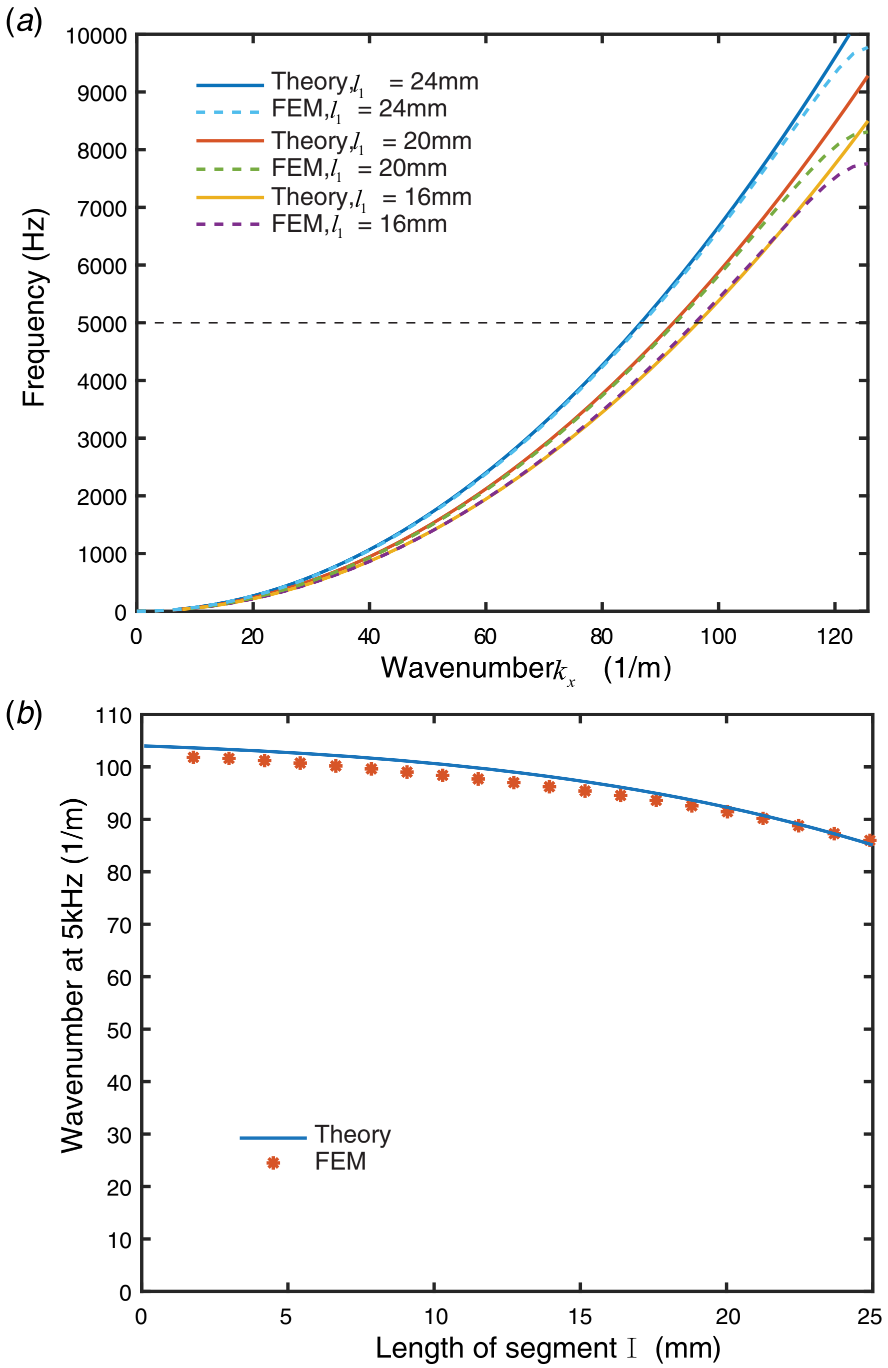

Fig. 3 (*a*) Dispersion relations of the unit cells with representative l_1 and (*b*) wavenumber of the unit cell at 5 kHz with various l_1

characteristics by modifying the dimension of the unit cell (Fig. 5(*a*)). Specifically, the characteristics of the phase shift of a single functional PC lane is analyzed at the operating frequency by sweeping the value of l_1 while keep h_2 at 2 mm. The phase shift characteristics of the elastic wave propagating through the lanes are obtained from the dispersion relation, as presented in Fig. 5(*b*).

It is shown in Fig. 5(*b*) that the phase shifts within the PC lanes decrease with respected to the increase of l_1. Moreover, the phase shift in the lane consisting one unit cell is quite limited. Connecting multiple identical unit cells in series can extend the range of phase shift effectively. For example, the PC lane assembled with ten unit cells yields a phase shift covering a full π range, i.e., the configured functional lane with ten unit cells meets the requirement for rendering the destructive interference perfectly. Besides, it can be obtained from Fig. 5(*c*) that for all the lanes with 1, 5, and 10 cells, we have all the values of transmission larger than −3 dB and most of the reflection ratio smaller than −20 dB. Therefore, we adopt PC lanes with ten unit cells assembled in a series to form the PC system with coupled lanes in the following analysis. It is worth mentioning that choosing a higher operating frequency can shorten the length of the elastic wave, i.e., the phase shift covering a full π range is potential to be achieved with much less unit cells.

We then assemble the functional units for realizing the destructive interference with two aforementioned PC lanes, as shown in Fig. 6(*a*). Perfectly matched layers (PMLs) are added to the both ends of the lanes, and a transverse wave is incident from the left end. Note that a PC plate is synthesized by many dual-lane

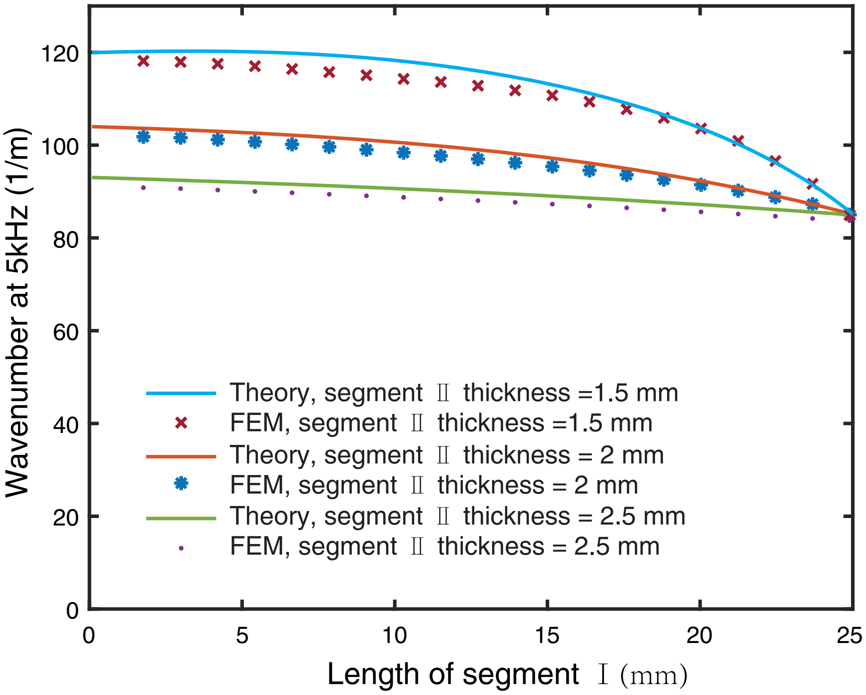

Fig. 4 Wavenumbers of the unit cells at 5 kHz with various l_1 and representative h_2

functional units arranged in y-direction, and a continuous boundary condition is applied laterally for a dual-lane functional unit. The three cases are evaluated where the h_2 of the unit cells is kept as 1.5 mm, 2 mm, and 2.5 mm, respectively, in both of the PC lanes. The phase difference between two lanes are obtained as shown in Fig. 6(*b*) by sweeping l_1 in one lane, while all the parameters of the other lane are kept constant (case 1.1: $h_2 = 1.5$ mm, $l_1 =$ 23 mm; case 1.2: $h_2 = 2$ mm, $l_1 l_1 = 23$ mm; case 1.3: $h_2 = 2.5$ mm, $l_1 = 23$ mm). Phase differences in the dual-lane functional units are analyzed by evaluating the responses in the far field.

It can be seen that in both case 1.1 and case 1.2 have a cumulative phase difference in a dual-lane unit covering the full range of π. It indicates that the functional units meet the requirement for rendering the destructive interference for wave attenuation. Moreover, reducing the value of h_2 can effectively enlarge the range of phase difference in a dual-lane unit. For example, the dual-lane functional unit with $h_2 = 2$ mm has a range of phase difference up to 4.75 rad. Besides, the maximum phase difference in the functional unit with $h_2 = 1.5$ mm is increased to 8.78 rad. Conversely, the functional unit with $h_2 = 2.5$ mm (case 1.3) yields a maximum phase difference of 2.01 rad because of the limited phase shift within a unit cell, as previously illustrated in Sec. 4.1. Theoretical calculations meet the FEM simulations well.

5 Elastic Wave Attenuation Characteristics

5.1 Attenuation Capability. In this section, the capability of wave attenuation of the proposed system is investigated. Since the dual-lane structure constitutes the basic unit that yields the phase difference for the potential wave attenuation, we evaluate the elastic wave attenuation features of the proposed system through analyzing the dual-lane functional unit first. Similarly, the continuous boundary condition is applied in y-direction. Here, three cases are considered. In particular, three dual-lane functional units are evaluated where the value of h_2 is chosen as 1.5 mm, 2 mm, and 2.5 mm, respectively. Besides, the dimensions of the unit cells in one of the lanes are kept constant in the three cases. The transmissions of the coupled PC beam as shown in Fig. 7 are obtained by sweep the value of l_1 in the other lane at 5 kHz.

Transmission diagrams of the dual-lane functional units at 5 kHz with different l_1 in one of the lanes are shown in Fig. 7(*a*). It can be observed that promising wave attenuation effect is obtained. Valleys of transmission are obtained at multiple values of l_1, e.g., $l_1 = 7.62$ mm and $l_1 = 20.58$ mm with $h_2 = 2$ mm. In the range of the valleys in the transmission diagrams, the elastic waves propagating through the dual-lane functional units have a phase difference that yields destructive interference and wave attenuation. Furthermore, the phase difference between the two lanes approximates π when $l_1 = 20.58$ mm as illustrated in Fig. 6(*b*) in Sec. 4.2. This phenomenon follows our proposed concept quite well that tailored phase difference in the dual-lane functional unit is capable of attenuating elastic waves significantly. Besides, the valley of the transmission at $l_1 = 7.62$ mm stems from the phase jump in one of the lanes. Furthermore, it can be obtained that the transmission curves of the dual-lane system with $h_2 = 1.5$ mm and $h_2 = 2$ mm have difference trends. This is because that the dual-lane system with $h_2 = 1.5$ mm has lowered Bragg Scatting bandgap and hence yield smaller transmission than that of the system with $h_2 = 2$ mm.

It can also be obtained from Fig. 7(*a*) that the transmission of the coupled PC lanes with $h_2 = 2.5$ mm has minor wave attenuation effect due to the limited phase difference yielded in the two lanes. Figure 7(*b*) shows the spatial responses for the cases with $l_1 =$ 7.62 mm and $l_1 = 20.58$ mm. It can be obtained that the design of the two lanes yields phase difference between the elastic waves. Besides, the waves transmitted through the two lanes meet at the end of the dual-lane section and cancel each other. In the near field, i.e., in the vicinity of the end of the dual-lane section, uneven displacement distribution can be observed due to the interaction of the two elastic waves. In the far field, the resultant displacements of the transmitted waves are minimized due to the superposition of two transmissions. In general, the final transmission is a superposition of two transmissions as a small gap is introduced between the two PC lanes as the case with $l_1 = 20.58$ mm. Conversely, the two lanes have small coupling with each other due to the near-field interactions. Thus, the case with $l_1 =$ 7.62 mm yields a phase jump at the entrance of the dual-lane section. It is worth emphasizing that, since the operating frequency is chosen below the Bragg scatting bandgap, the significant wave

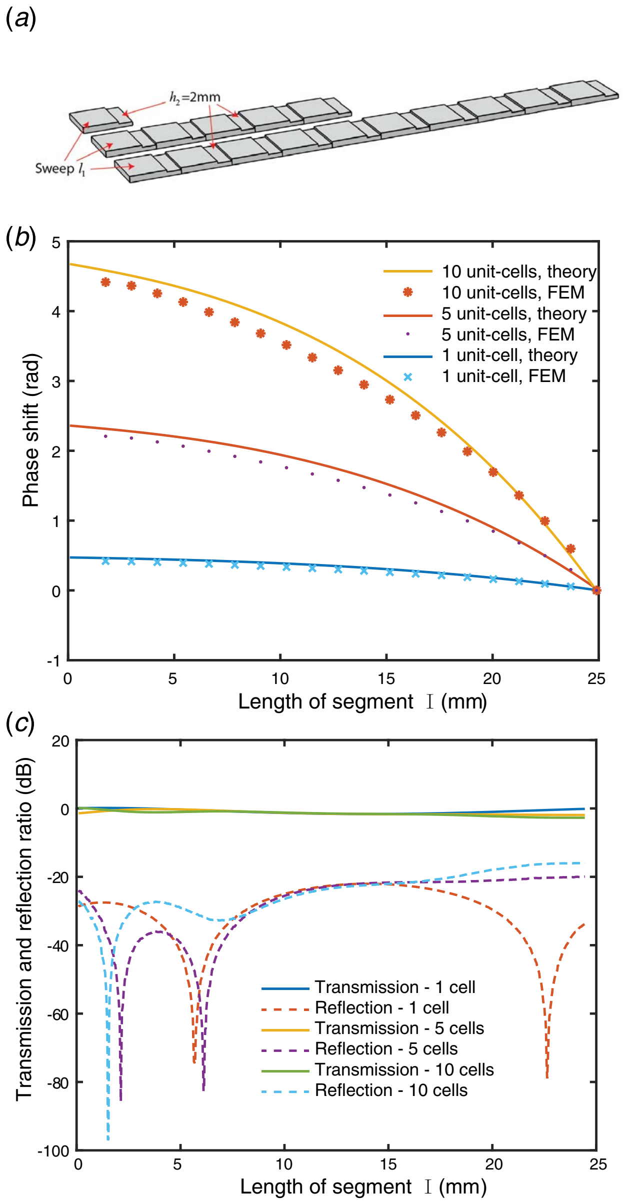

Fig. 5 (*a*) Configuration of PC lanes with multiple unit cells, (*b*) phase shift within a lane, and (c) transmission and reflection of a lane with $h_2 = 2$ mm at 5 kHz

attenuation phenomenon here is indeed induced by the mechanism of destructive interference. Since that the dual-lane PC unit with $h_2 = 2.5$ mm has the minor wave attenuation effect, we focus on the PC with $h_2 = 2$ mm and 1.5 mm in the following analysis.

5.2 Frequency Responses. The wave attenuation effect stems from the phase difference between PC lanes at a chosen frequency. To further demonstrate the robustness of the proposed design in a wide frequency range, frequency responses are plotted. Similarly, we first evaluate the elastic wave attenuation features of the PC system with coupled lanes through analyzing the dual-lane beam with continuous boundary conditions. Two cases are investigated with optimal parameters combination, i.e., case 2.1: $h_2 = 1.5$ mm, $l_1 = 7.71$ mm in one of the lanes in the dual-lane unit and $h_2 = 1.5$ mm, $l_1 = 23$ mm in the other; case 2.2: $h_2 = 2$ mm, $l_1 = 20.58$ mm in one of the lanes in the dual-lane unit and $h_2 = 2$ mm and $l_1 = 23$ mm in the other. Besides, the parameters of the unit cells are kept constant in one of the coupled lanes.

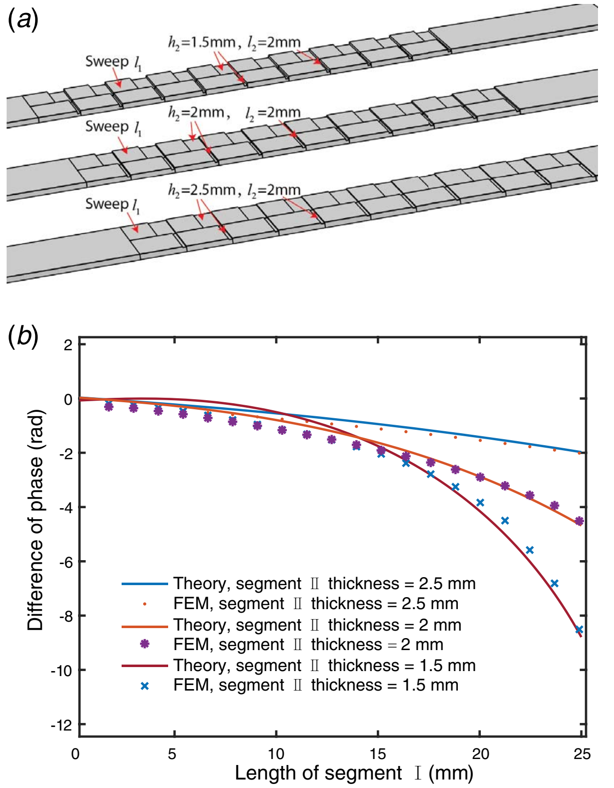

Fig. 6 (*a*) Dual-lane functional unit in PC plate and (*b*) phase difference in the dual-lane functional unit

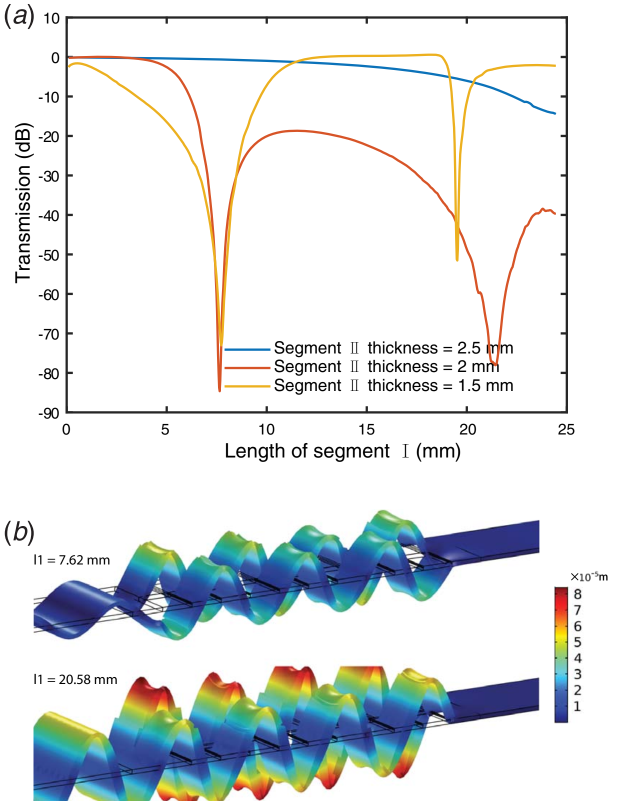

Fig. 7 (*a*) Transmission diagram of dual-lane units at 5 kHz and (*b*) spatial responses for $l_1 = 7.62$ mm and $l_1 = 20.58$ mm with $h_2 = 2$ mm

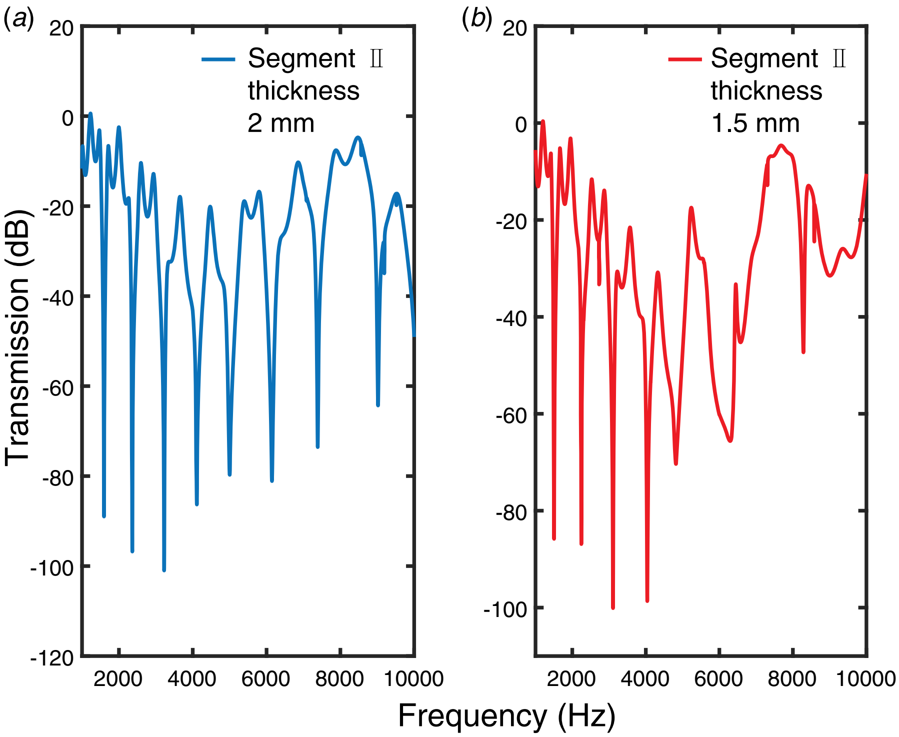

Fig. 8 (*a*) Transmission diagrams of dual-lane unit with $h_2 = 2$ mm and (*b*) transmission diagrams of dual-lane unit with $h_2 = 1.5$ mm

The transmission diagrams are calculated through the following equation:

$$\text{trans}(\omega) = 20\log_{10}\frac{A_{\text{transmitted}}(\omega)}{A_{\text{incident}}(\omega)} \tag{13}$$

where $A_{\text{transmitted}}(\omega)$ and $A_{\text{incident}}(\omega)$ are the amplitudes of the signals of the transmitted and incident elastic waves resolved at frequency ω, respectively. Corresponding transmission diagrams in frequency domain are shown in Fig. 8.

It can be seen from Fig. 8 that pronounced wave attenuation is achieved at 5 kHz and many other frequency points in a large frequency range from 1 kHz to 10 kHz. In this frequency range, the wave attenuation effect is induced by the same underlying physics, that is, the elastic wave undergoes phase difference rendered self-cancellation. It is worth noticing that the first valley in the transmission diagram is as low as 1.85 kHz. Moreover, the spatial responses of the dual-lane functional unit with $h_2 = 2$ mm at 2.37 kHz, 5.00 kHz, and 8.73 kHz are plotted in Fig. 9, representing three valleys in the transmission diagram. It can be observed that significant wave attenuation effects can be observed. At the points of the minimal values of the transmission, the phase difference between the waves in the two lanes approximates π. Among which the spatial response of the dual-lane functional unit at 8.73 kHz shows uneven displacements at the right end of the dual-lane section. This phenomenon can be attributed to the high bending strain in near-field range yielded by the accumulated waves. Nevertheless, the elastic waves are attenuated in far field ranges. In consideration that vibrations at multiple frequencies would be attenuated at the same time, the proposed system provides a significant flexibility in devising wave attenuation systems with varying operating frequencies through proper parameter selection.

We further synthesize the PC plate with the aforementioned dual-lane functional units. In this plate, the dual-lane functional units are periodically arranged in y-direction. Here, we consider PC plate consisting unit cells with $h_2 = 2$ mm. Besides, the value of l_1 is chosen as 23 mm in one lane of the dual-lane unit and 20.58 mm in the other one. PMLs are added to the both ends of the beam and a transverse harmonic wave with the width of 350 mm is incident from the left end. Here, the PMLs on the two sides are artificial absorbing layers for minimizing the reflection of the elastic waves at the two sides and reveal the wave manipulation characteristics of the phononic plate. Responses of the plate at representative frequency points are obtained, as shown in Fig. 10.

Figure 10 shows that significant wave attenuation is achieved in the proposed PC plate with coupled lanes due to the destructive interference at multiple frequency points. The enhanced wave attenuation capability follows the prediction in Fig. 8 well. This robustness has great potential in vibration attenuations where large-range low-frequency attenuation is desired. Unlike the metamaterials employing local resonators working at a single frequency, the proposed low-frequency wave attenuation mechanism is realized by destructive interference through phase modulation. The features of wide band wave attenuation can be attributed to the fact that the PC has much smaller phase changes in the frequency range

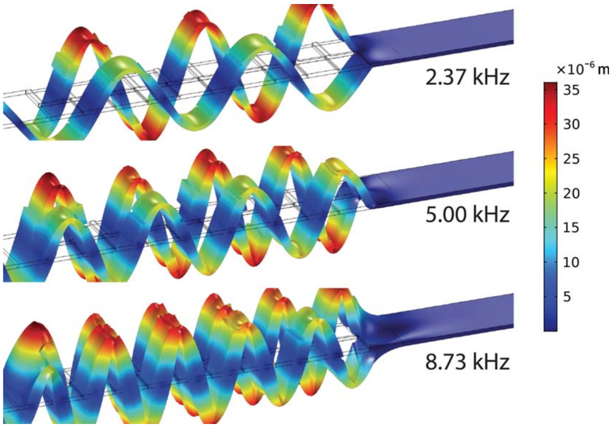

Fig. 9 Spatial responses of the dual-lane functional unit at 2.37 kHz, 5.00 kHz, and 8.73 kHz

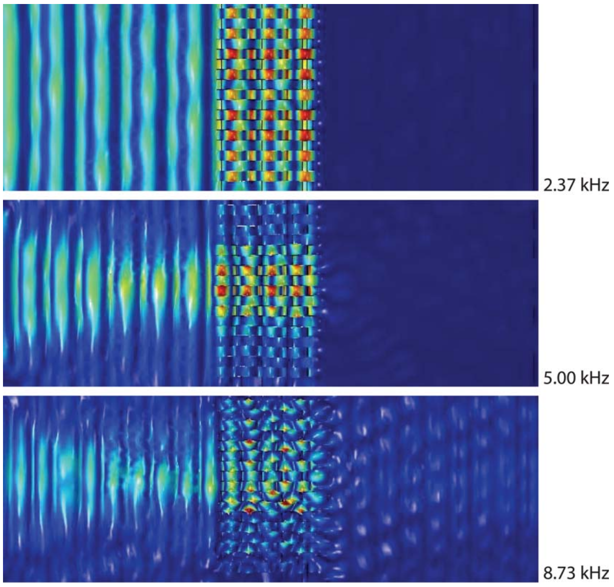

Fig. 10 Spatial responses of the plate at 2.37 kHz, 5.00 kHz, and 8.73 kHz

than that in the local resonator-based metamaterials. In this study, PC with stair-shaped unit cell is adopted to illustrate the proposed concept. The proposed system can also be synthesized with piezoelectric transducers and shunting circuits to achieve online tunability.

5.3 Comparison and Discussion. For further illustration of the proposed concept, frequency response of the PCs with coupled lanes is compared with traditional PCs. Two additional cases corresponding to traditional phononic crystals are considered. In the comparison, the proposed phononic crystals with coupled lanes having dimensions follow the case illustrated in Sec. 5.2. Besides, the two traditional PCs have similar configurations of the proposed system where one of them has $h_2 = 2$ mm, $l_1 = 20.58$ mm, and the other one has $h_2 = 1.5$ mm, $l_1 = 7.71$ mm. They represent traditional phononic crystal beams with Bragg scattering bandgaps. The corresponding transmission curves of the comparison of the proposed system and traditional PC are shown in Fig. 11.

Figure 11 shows the comparison between the proposed systems and the traditional PCs. It can be obtained that the traditional PC with the parameter combination has no bandgap in the frequency range of interest with $h_2 = 2$ mm. Meanwhile, the proposed PC with coupled lanes exhibits promising wave attenuation capability in a wide frequency range of interest. It confirms the feature of the proposed system that phase difference enables the PC with the capability of wave attenuation over a large frequency range. Notably, the proposed system has valley of transmission diagrams at 1.85 kHz. This low-frequency wave attenuation capability was considered as the unique feature of local resonators-based metamaterials. In particular, the proposed system illustrates an advantage that it has deep valleys in the transmission diagram in multiple frequency points, while the local resonance-based metamaterial has only one valley in the vicinity of local resonance. Conversely, the proposed method requires more than one lane to achieve such a wave attenuation. In addition, the traditional PC with $h_2 = 1.5$ mm has a bandgap in the frequency range of 6 kHz–10 kHz. Specifically, the proposed system with $h_2 = 1.5$ mm has multiple frequency ranges, which sum up to 7839.9 Hz with more than 10 dB attenuation. As for comparison, the conventional phononic crystal (shown in Fig. 11(*b*)) only has a frequency range up to 4245 Hz to achieve 10 dB attenuation. Moreover, if the attenuation criterion is increased to 20 dB, the bandwidths of the proposed system and the conventional one are 6225.7 Hz and 3948 Hz, respectively. That is, the proposed system has much wider frequency range of wave attenuation than the conventional phononic crystal. Furthermore, the traditional PC system shows limited wave attenuation capacity, i.e., it has valleys in the transmissions of −56.34 dB. Conversely, the proposed PC system has much deeper valleys in the lower frequency range. Specifically, the proposed system has a

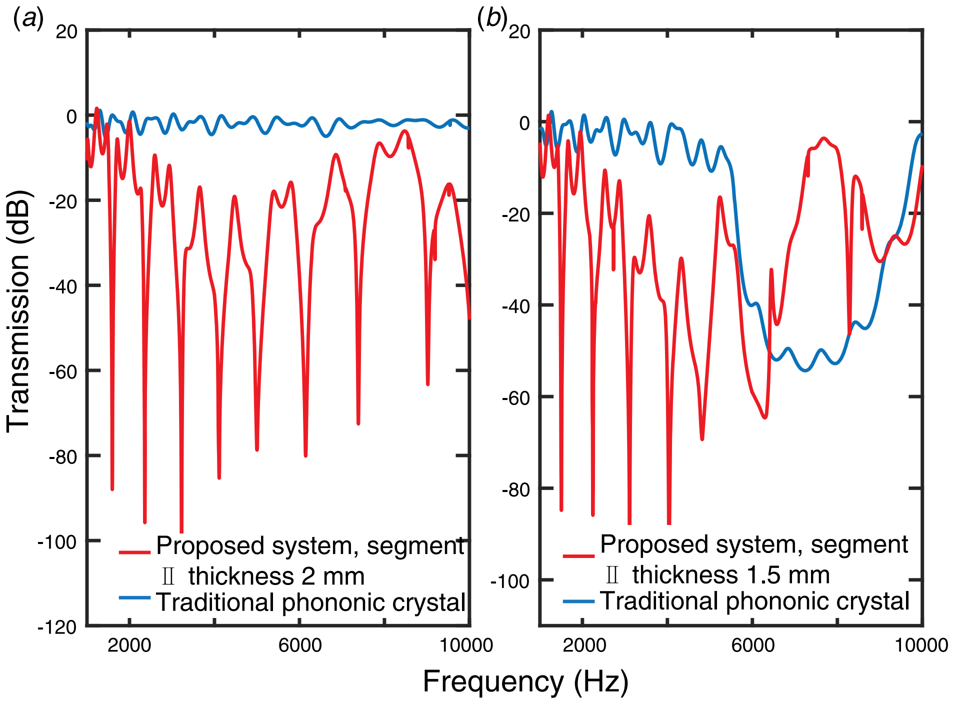

Fig. 11 Comparison of transmission diagrams of proposed PC with coupled lanes and traditional PC: (*a*) $h_2 = 2$ mm and (*b*) $h_2 = 1.5$ mm

maximum wave attenuation capacity of −86.7 dB, which significantly outperforms the traditional one. Consider that local resonance-based metamaterials are potential to attenuation wave more than −60 dB [23,29,39–42], the proposed system has a wave attenuation capacity on the same level as that of the metamaterials. These results confirm the feasibility of the proposed system for wave attenuation in a wider and much lower frequency range than that of the traditional PCs.

6 Conclusions

In summary, a PC plate based on the mechanism of destructive interference for enhanced wave attenuation is demonstrated. The PC plate is designed using dual-lane functional units integrated with stair-shaped unit cells. A Euler–Bernoulli beam model is formulated, and FEM simulations are presented. The phase shift characteristics of the unit cell, and the functional PC lanes are analyzed in detail. It is demonstrated that under a given operating frequency of interest, we can facilitate phase difference covering full π range in a dual-lane functional unit with proper selection of the dimension of the unit cells. The phase difference in the vicinity of π in the dual-lane unit yields wave attenuation of the waves owing to destructive interference. We further demonstrate the significant wave attenuation capability of the proposed system in the low-frequency range, which outperforms the traditional PC in a wide frequency range with better attenuation capacity. The results show that multiple valleys in the transmission can be achieved between 1 kHz and 10 kHz with one at a frequency as low as 1.85 kHz with unit cells' width and length of 25 mm and ten unit cells in one lane. The proposed PC system with coupled lanes has promising potential for low-frequency broadband wave attenuation.

Funding Data

- National Key Technologies R&D Program (Grants Nos. 2019YFC0119303 and 2019YFC0119304; Funder ID: 10.13039/501100011291).
- National Natural Science Foundation of China (Grant No. 6522007289; Funder ID: 10.13039/501100001809).
- Natural Science Foundation of Jiangsu Province (Grant No. 7722009004; Funder ID: 10.13039/501100004608).

Conflict of Interest

There are no conflicts of interest.

References

[1] Liu, Z., Zhang, X., Mao, Y., Zhu, Y. Y., Yang, Z., Chan, C. T., and Sheng, P., 2000, "Locally Resonant Sonic Materials," Science, **289**(5485), pp. 1734–1736.

[2] Fang, N., Lee, H., Sun, C., and Zhang, X., 2005, "Sub-Diffraction-Limited Optical Imaging With a Silver Superlens," Science, **308**(5721), p. 534.

[3] Pendry, J. B., and Li, J., 2008, "An Acoustic Metafluid: Realizing a Broadband Acoustic Cloak," New J. Phys., **10**(11), p. 115032.

[4] Landy, N. I., Sajuyigbe, S., Mock, J. J., Smith, D. R., and Padilla, W. J., 2008, "Perfect Metamaterial Absorber," Phys. Rev. Lett., **100**(20), p. 207402.

[5] Yang, J., Huang, M., Yang, C., Peng, J., and Chang, J., 2010, "An External Acoustic Cloak With N-Sided Regular Polygonal Cross Section Based on Complementary Medium," Comput. Mater. Sci., **49**(1), pp. 9–14.

[6] Bigoni, D., Guenneau, S., Movchan, A. B., and Brun, M., 2013, "Elastic Metamaterials With Inertial Locally Resonant Structures: Application to Lensing and Localization," Phys. Rev. B, **87**(17), p. 174303.

[7] Baravelli, E., and Ruzzene, M., 2013, "Internally Resonating Lattices for Bandgap Generation and Low-Frequency Vibration Control," J. Sound Vib., **332**(25), pp. 6562–6579.

[8] Yoo, Y. J., Zheng, H. Y., Kim, Y. J., Rhee, J. Y., Kang, J.-H., Kim, K. W., Cheong, H., Kim, Y. H., and Lee, Y. P., 2014, "Flexible and Elastic Metamaterial Absorber for Low Frequency, Based on Small-Size Unit Cell," Appl. Phys. Lett., **105**(4), p. 041902.

[9] Pendry, J. B., 2000, "Negative Refraction Makes a Perfect Lens," Phys. Rev. Lett., **85**(18), p. 3966.

[10] Li, J., and Chan, C. T., 2004, "Double-Negative Acoustic Metamaterial," Phys. Rev. E, **70**(5), p. 055602.

[11] Climente, A., Torrent, D., and Sanchez-Dehesa, J., 2010, "Sound Focusing by Gradient Index Sonic Lenses," Appl. Phys. Lett., **97**(10), p. 104103.

[12] Wu, T.-T., Chen, Y.-T., Sun, J.-H., Lin, S. S., and Huang, T. J., 2011, "Focusing of the Lowest Antisymmetric Lamb Wave in a Gradient-Index Phononic Crystal Plate," Appl. Phys. Lett., **98**(17), p. 171911.

[13] Zhao, J., Marchal, R., Bonello, B., and Boyko, O., 2012, "Efficient Focalization of Antisymmetric Lamb Wave in Gradient-Index Phononic Crystal Plates," Appl. Phys. Lett., **101**(26), p. 261905.

[14] Yan, X., Zhu, R., Huang, G., and Yuan, F.-G., 2013, "Focusing Guided Waves Using Surface Bonded Elastic Metamaterials," Appl. Phys. Lett., **103**(12), p. 121901.

[15] Tol, S., Degertekin, F. L., and Erturk, A., 2016, "Gradient Index Phononic Crystal Lens-Based Enhancement of Elastic Wave Energy Harvesting," Appl. Phys. Lett., **109**(6), p. 063902.

[16] Beck, B. S., Cunefare, K. A., Ruzzene, M., and Collet, M., 2011, "Experimental Analysis of a Cantilever Beam With a Shunted Piezoelectric Periodic Array," J. Intell. Mater. Syst. Struct., **22**(11), pp. 1177–1187.

[17] Xu, J., Li, S., and Tang, J., 2018, "Customized Shaping of Vibration Modes by Acoustic Metamaterial Synthesis," Smart Mater. Struct., **27**(4), p. 045001.

[18] Yang, Z., Mei, J., Yang, M., Chan, N. H., and Sheng, P., 2008, "Membrane-Type Acoustic Metamaterial With Negative Dynamic Mass," Phys. Rev. Lett., **101**(20), p. 204301.

[19] Mei, J., Ma, G., Yang, M., Yang, Z., Wen, W., and Sheng, P., 2012, "Dark Acoustic Metamaterials as Super Absorbers for Low-Frequency Sound," Nat. Commun., **3**(1), p. 756.

[20] Kushwaha, M. S., Halevi, P., Dobrzynski, L., and Djafari-Rouhani, B., 1993, "Acoustic Band Structure of Periodic Elastic Composites," Phys. Rev. Lett., **71**(13), p. 2022.

[21] Monsoriu, J. A., Depine, R. A., MartÝnez-Ricci, M. L., and Silvestre, E., 2006, "Interaction Between Non-Bragg Band Gaps in 1D Metamaterial Photonic Crystals," Opt. Express, **14**(26), pp. 12958–12967.

[22] Airoldi, L., and Ruzzene, M., 2011, "Wave Propagation Control in Beams Through Periodic Multi-Branch Shunts," J. Intell. Mater. Syst. Struct., **22**(14), p. 1567.

[23] Huang, G. L., and Sun, C. T., 2010, "Band Gaps in a Multiresonator Acoustic Metamaterial," ASME J. Vib. Acoust., **132**(3), p. 031003.

[24] Tan, K. T., Huang, H. H., and Sun, C. T., 2014, "Blast-Wave Impact Mitigation Using Negative Effective Mass Density Concept of Elastic Metamaterials," Int. J. Impact Eng., **64**, pp. 20–29.

[25] Xu, J., and Tang, J., 2017, "Tunable Prism Based on Piezoelectric Metamaterial for Acoustic Beam Steering," Appl. Phys. Lett., **110**(18), p. 181902.

[26] Xiao, Y., Wen, J., and Wen, X., 2012, "Longitudinal Wave Band Gaps in Metamaterial-Based Elastic Rods Containing Multi-Degree-of-Freedom Resonators," New J. Phys., **14**(3), p. 033042.

[27] Li, Y., Liang, B., Gu, Z., Zou, X., and Cheng, J., 2013, "Reflected Wavefront Manipulation Based on Ultrathin Planar Acoustic Metasurfaces," Sci. Rep., **3**(1), p. 2546.

[28] Chen, Y. Y., Huang, G. L., and Sun, C. T., 2014, "Band Gap Control in an Active Elastic Metamaterial With Negative Capacitance Piezoelectric Shunting," ASME J. Vib. Acoust., **136**(6), p. 061008.

[29] Thorp, O., Ruzzene, M., and Baz, A., 2001, "Attenuation and Localization of Wave Propagation in Rods With Periodic Shunted Piezoelectric Patches," Smart Mater. Struct., **10**(5), p. 979.

[30] Li, Y., Jiang, X., Li, R., Liang, B., Zou, X., Yin, L., and Cheng, J., 2014, "Experimental Realization of Full Control of Reflected Waves With Subwavelength Acoustic Metasurfaces," Phys. Rev. Appl., **2**(6), p. 064002.

[31] Xie, Y., Wang, W., Chen, H., Konneker, A., Popa, B. I., and Cummer, S. A., 2014, "Wavefront Modulation and Subwavelength Diffractive Acoustics With an Acoustic Metasurface," Nat. Commun., **5**(1), p. 5553.

[32] Tang, K., Qiu, C., Ke, M., Lu, J., Ye, Y., and Liu, Z., 2014, "Anomalous Refraction of Airborne Sound Through Ultrathin Metasurfaces," Sci. Rep., **4**(1), p. 6517.

[33] Yuan, B., Cheng, Y., and Liu, X., 2015, "Conversion of Sound Radiation Pattern via Gradient Acoustic Metasurface With Space-Coiling Structure," Appl. Phys. Express, **8**(2), p. 027301.

[34] Li, Y., Jiang, X., Liang, B., Cheng, J., and Zhang, L., 2015, "Metascreen-Based Acoustic Passive Phased Array," Phys. Rev. Appl., **4**(2), p. 024003.

[35] Ma, G., and Sheng, P., 2016, "Acoustic Metamaterials: From Local Resonances to Broad Horizons," Sci. Adv., **2**(2), p. e1501595.

[36] Zhu, H., and Semperlotti, F., 2016, "Anomalous Refraction of Acoustic Guided Waves in Solids With Geometrically Tapered Metasurfaces," Phys. Rev. Lett., **117**(3), p. 034302.

[37] Liu, Y., Liang, Z., Liu, F., Diba, O., Lamb, A., and Li, J., 2017, "Source Illusion Devices for Flexural Lamb Waves Using Elastic Metasurfaces," Phys. Rev. Lett., **119**(3), p. 034301.

[38] Su, X., Lu, Z., and Norris, A. N., 2018, "Elastic Metasurfaces for Splitting SV- and P-Waves in Elastic Solids," J. Appl. Phys., **123**(9), p. 091701.

[39] Hu, G., Tang, L., Das, R., Gao, S., and Liu, H., 2017, "Acoustic Metamaterials With Coupled Local Resonators for Broadband Vibration Suppression," AIP Adv., **7**(2), p. 025211.

[40] Xu, J., Yan, R., and Tang, J., 2018, "Broadening Bandgap Width of Piezoelectric Metamaterial by Introducing Cavity," Appl. Sci., **8**(9), p. 1606.

[41] Fang, X., Wen, J., Bonello, B., Yin, J., and Yu, D., 2017, "Ultra-Low and Ultra-Broad-Band Nonlinear Acoustic Metamaterials," Nat. Commun., **8**(1), p. 1288.

[42] Khajehtourian, R., and Hussein, M., 2014, "Dispersion Characteristics of a Nonlinear Elastic Metamaterial," AIP Adv., **4**(12), p. 124308.

[43] Lazarov, B. S., and Jensen, J. S., 2007, "Low-Frequency Band Gaps in Chains With Attached Non-Linear Oscillators," Int. J. Non-Linear Mech., **42**(10), pp. 1186–1193.

[44] Lee, W.-S., Kim, D.-Z., Kim, K.-J., and Yu, J.-W., 2006, "Wideband Planar Monopole Antennas With Dual Band-Notched Characteristics," IEEE Trans. Microwave Theory Tech., **54**(6), pp. 2800–2806.

[45] Oh, T., Lim, Y.-G., Chae, C.-B., and Lee, Y., 2015, "Dual-Polarization Slot Antenna With High Cross-Polarization Discrimination for Indoor Small-Cell MIMO Systems," IEEE Antennas Wireless Propagation Lett., **14**(1), pp. 374–377.

[46] Deymier, P., 2013, *Acoustic Metamaterials and Phononic Crystals*, Springer, Berlin/Heidelberg, Germany.

[47] Xu, J., Zhang, X., and Yan, R., 2020, "Coupled Piezoelectric Phononic Crystal for Adaptive Broadband Wave Attenuation by Destructive Interference," ASME J. Appl. Mech., **87**(9), p. 091001.

[48] Zhu, R., Liu, X., Hu, G., Sun, C., and Huang, G., 2014, "A Chiral Elastic Metamaterial Beam for Broadband Vibration Suppression," J. Sound Vib., **333**(10), pp. 2759–2773.